



저작자표시-비영리-변경금지 2.0 대한민국

이용자는 아래의 조건을 따르는 경우에 한하여 자유롭게

- 이 저작물을 복제, 배포, 전송, 전시, 공연 및 방송할 수 있습니다.

다음과 같은 조건을 따라야 합니다:



저작자표시. 귀하는 원저작자를 표시하여야 합니다.



비영리. 귀하는 이 저작물을 영리 목적으로 이용할 수 없습니다.



변경금지. 귀하는 이 저작물을 개작, 변형 또는 가공할 수 없습니다.

- 귀하는, 이 저작물의 재이용이나 배포의 경우, 이 저작물에 적용된 이용허락조건을 명확하게 나타내어야 합니다.
- 저작권자로부터 별도의 허가를 받으면 이러한 조건들은 적용되지 않습니다.

저작권법에 따른 이용자의 권리는 위의 내용에 의하여 영향을 받지 않습니다.

이것은 [이용허락규약\(Legal Code\)](#)을 이해하기 쉽게 요약한 것입니다.

[Disclaimer](#)

이학석사 학위논문

**Magnetic proximity effect in $\text{MoSe}_2/\text{CrBr}_3$
heterostructures**

$\text{MoSe}_2/\text{CrBr}_3$ 이중접합구조에서
자기 근접효과

2022년 8월

서울대학교 대학원

물리천문학부

이 은 호

Magnetic proximity effect in $\text{MoSe}_2/\text{CrBr}_3$ heterostructures

$\text{MoSe}_2/\text{CrBr}_3$ 이중접합구조에서
자기 근접효과

지도교수 최현용

이 논문을 이학석사 학위논문으로 제출함
2022년 8월
서울대학교 대학원
물리천문학부
이 은 호

이은호의 이학석사 학위논문을 인준함
2022년 8월

위 원 장 _____ 김 도 현 (인)

부위원장 _____ 최 현 용 (인)

위 원 _____ 이 지 은 (인)

Abstract

Combining two-dimensional magnet and transition metal dichalcogenide into van der Waals heterostructures enables control of valley degree of freedom with additional means and presents a promising platform for data processing and storage based on opto-valleytronic materials. In this study, we fabricated van der Waals heterostructures by interfacing a monolayer MoSe_2 and a few layered CrBr_3 . Through measurements of the power-dependent photoluminescence spectrum, we assigned the two observed resonances as positive trion and exciton respectively. We performed magneto-photoluminescence measurements under the heterostructures in a circular-polarization-resolved configuration and observed that the valley polarization of the MoSe_2 trion resonance follows the CrBr_3 magnetization. This can be explained by spin-dependent interlayer charge transfer between MoSe_2 and CrBr_3 . The gate-dependent reflection contrast spectrum corroborates the type-II band alignment. We found evidence for unexpected antiferromagnetic coupling in CrBr_3 through photoluminescence and magnetic circular dichroism measurements in $\text{MoSe}_2/\text{CrBr}_3$ heterostructures, and it needs to be further investigated.

To evaluate the carrier dynamics in the heterostructures, we performed the transient reflectivity and time-resolved Kerr rotation measurements. Valley depolarization time was estimated to be less than 1 ps, which precedes the radiative lifetime of trion and exciton. The Kerr rotation signal of the residual valley hole generated from the spin-dependent charge transfer could not be resolved.

Keywords: Magnetic proximity effect, Heterostructures,
Magneto-photoluminescence, Magnetic circular
dichroism, Kerr rotation, MoSe_2 , CrBr_3

Student number: 2020-28149

Table of Contents

Abstract	i
List of Figures.....	iv
Chapter 1. Introduction.....	1
1.1 Motivation and Outline of Research	1
Chapter 2. Background Information.....	2
2.1 Two-dimensional Transition Metal Dichalcogenides ..	2
2.2 van der Waals Magnets.....	6
Chapter 3. Methods.....	9
3.1 Device Fabrication.....	9
3.2 PL, RC and MCD Measurements	11
3.3 TR and TR-KR Measurements.....	16
Chapter 4. Magnetic proximity effect in MoSe ₂ /CrBr ₃ Heterostructures.....	19
4.1 Type-II Band Alignment and Spin-selective Charge Transfer	19
4.2 Antiferromagnet-like Switching and Charge Transfer- dominated DOCP	27
Chapter 5. Ultrafast studies on carrier dynamics in MoSe ₂ /CrBr ₃ Heterostructures	31
5.1 TR Measurements.....	31
5.2 TR-KR Measurements	32
Chapter 6. Conclusion.....	34
Bibliography	35
국문초록.....	39

List of Figures

Figure 1 a. The trigonal prism coordination geometry of 2H phase TMD. b. Top view of 2H phase TMD monolayer. c. Schematics of the spin–valley locked band edges in monolayer WX_2	3
Figure 2 a. Schematics of excitons in real space and optical absorption spectra in 2D & 3D cases. b. Gate dependent PL of monolayer WSe_2	6
Figure 3 a. Electron spin configuration in d orbital of Cr^{3+} in CrX_3 . b. Schematics for intralayer super–exchange interaction in CrX_3 . c. Circular–polarization–resolved reflection contrast spectrum of tri–layer CrI_3	8
Figure 4 Optical microscope images for device fabrication steps. White scale bars represent $20\ \mu m$. a. Transfer of bottom hBN. b. Transfer of FLG. c. Electron beam lithography and development of PMMA resist. d. Thermal evaporation of Ti/Au contact and lift–off. e. Exfoliation of monolayer $MoSe_2$. f. Transfer of top hBN. g. Pick up of $CrBr_3$. h. Finished device.	10
Figure 5 Schematics of an experimental setup for a magnetic–field–dependent circular–polarization–resolved PL. LP: linear polarizer, DM: dichroic mirror, SM: scanning mirror, SL: scan lens, TL: tube lens, BS: beam splitter....	15
Figure 6 a. Schematics of an experimental setup for MCD measurements. LP: linear polarizer, DM: dielectric mirror. b. Quarter–wave polarization modulation and boxcar averaging scheme with A, B gates..	16
Figure 7 a. Schematics of an experimental setup for TR measurements. b. Schematics of an experimental setup for TR–KR measurements.....	18

Figure 8 a. Optical microscope image of device #1. b. SPCM scan image of total PL signal. c. Schematics of band alignments and photodoping mechanism. d. PL spectra of monolayer MoSe ₂ and MoSe ₂ /CrBr ₃ heterostructures. e. Power-dependent PL spectra of MoSe ₂ /CrBr ₃ heterostructures.	21
Figure 9 Magnetic-field-dependent circular-polarization-resolved PL of an upward sweep. a. PL map in R/R and R/L configuration. b. DOCP map in R and L excitation.	23
Figure 10 a. Schematics of spin-dependent charge transfer from MoSe ₂ into CrBr ₃ . b. Magnetic-field-dependent DOCP of trion and exciton with R excitation and L excitation. c. Magnetic-field-dependent valley splitting of trion and exciton with R excitation and L excitation.	25
Figure 11 SPCM scan image of DOCP of total PL signal. .	26
Figure 12 a. Gate-dependent RC spectrum of monolayer MoSe ₂ . b. Circular polarized resolved RC spectrum of MoSe ₂ /CrBr ₃ heterostructures at $B = 200$ mT. c. Gate-dependent RC spectrum of MoSe ₂ /CrBr ₃ heterostructures at $B = 200$ mT.	27
Figure 13 a. Optical microscope image of device #2. b. SPCM scan image of total PL signal. c. DOCP map with linear polarized excitation. d. Magnetic-field-dependent DOCP and valley splitting of trion and exciton with linear polarized excitation.	28
Figure 14 a. MCD hysteresis loop. b. PL DOCP map with linear polarized excitation for several magnetic fields.	29
Figure 15 Large-field-dependent a. PL DOCP and b. valley splitting.	30
Figure 16 a. TR spectrum for monolayer MoSe ₂ . b. RC	

spectrum raw data and one modified by TR spectrum at $t = 1$ ps for monolayer MoSe₂. c. TR at low energy wing of exciton resonance for monolayer MoSe₂. d–f. Figures of the same forms with a–c for MoSe₂/CrBr₃

heterostructures..... 32

Figure 17 a. Raw data of time–delay–dependent auto–balanced signal. b. differential TR–KR for monolayer MoSe₂. c. differential TR–KR for MoSe₂/CrBr₃

heterostructures. 33

Chapter 1. Introduction

1.1. Motivation and Outline of Research

The proximity effect in heterostructures of van der Waals semiconductors and magnetic materials has been intensively studied and various material pairs have been presented. The magnetic proximity effect for monolayer transition metal dichalcogenides (TMD) can be a powerful tool to connect electronics, optics, and magnetism, due to its semiconductive property and strong excitonic optical response. Thanks to atomically flatness, the van der Waals heterostructures of the monolayer TMD interfaced with a van der Waals magnet are suitable for such purposes. For example, exchange-coupling-induced valley Zeeman splitting up to 3.5 meV was reported for $\text{WSe}_2/\text{CrI}_3$ heterostructures without any applied magnetic field, which is equivalent to an effective magnetic field of 13 T [1]. In addition, by introducing a semiconductive magnet, one can control the spin-dependent interlayer tunneling rate.

In this study, we fabricated $\text{MoSe}_2/\text{CrBr}_3$ van der Waals heterostructures in a transistor form, and perform magneto-photoluminescence measurements so that we could confirm the magnetic proximity effect previously reported for the same material pair [2]. Through time-resolved studies, we found that the valley depolarization precedes other dynamics: exciton & trion radiative recombination in MoSe_2 and electron transfer from MoSe_2 to CrBr_3 .

Chapter 2. Background Information

2.1. Two-dimensional Transition Metal Dichalcogenides

TMD refers to a class of van der Waals materials with the chemical formula MX_2 , where M is a transition metal atom and X is a chalcogen atom. TMDs show a wide range of physical properties, such as superconductivity in NbSe_2 [3] or MoS_2 [4], quantum spin Hall effect in WTe_2 [5], and various kinds of exciton complexes in monolayer WSe_2 [6]. In this study, we particularly focus on the group VI TMD in the 2H phase monolayer form which shows a strong excitonic optical resonance and electronic tunability of it.

2.1.1. Electronic Structure of TMD

2H phase corresponds to the trigonal prismatic coordination of transition metal atoms. From a top view of the monolayer along the c -axis, one can notice that this is the ABA stacking of the triangular lattice of chalcogen, metal, and chalcogen atoms. It has the form of a hexagonal lattice with broken inversion symmetry in total. Compared to graphene, the electronic structure of the 2H phase TMD monolayer consists of a massive Dirac Hamiltonian near the K symmetry point. Due to strong spin-orbit coupling (SOC) originating from the heavy transition metal atoms, the valence and conduction bands of it are

spin-split. Horizontal mirror planes imply that the direction of split spin is out-of-plane and time reversal symmetry makes spin-splitting directions in the inequivalent two valleys mutually opposite. TMD in monolayer form has a direct band gap at K symmetry points, so the spin-valley locking, which has been explained above, and optical selection rule plus the excitonic effect that will be explained below make this class of materials a promising optoelectronic platform.

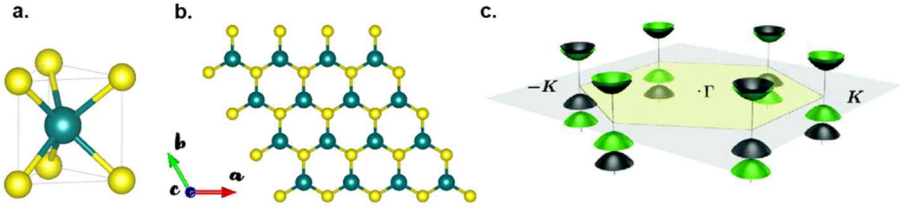


Figure 18 a. The trigonal prism coordination geometry of 2H phase TMD. b. Top view of 2H phase TMD monolayer. c. Schematics of the spin-valley locked band edges in monolayer WX_2 [7].

2.1.2. Optical Selection Rule of Monolayer TMD

Considering the intra-atomic SOC of transition metal d orbitals, the effective Hamiltonian can be written as following near the K symmetry point on the Brillouin zone edge using k -p mode [8]:

$$\hat{H}_{k-p}(k) = at(\tau k_x \hat{\sigma}_x + k_y \hat{\sigma}_y) + \frac{\Delta}{2} \hat{\sigma}_y - \lambda_v \tau s_z \frac{\hat{\sigma}_z - 1}{2}$$

where a is the lattice constant, t is the hopping parameter, $\tau = \pm 1$ is the valley index, Δ is the energy gap, λ_v is the valance band energy splitting, and $\hat{\sigma}$ is the Pauli matrices. The

first term resembles the massless Dirac Hamiltonian for graphene. The second term represents the mass term explaining the opened gap. The third term is introduced to explain the spin-splitting of the valence band due to the SOC of transition metal atoms.

Because the two-band Hamiltonian above is just a 2 by 2 Hermitian matrix, we can easily diagonalize it with the basis of the following:

$$|u_c\rangle = \begin{pmatrix} \cos \frac{\theta}{2} \\ e^{i\varphi} \sin \frac{\theta}{2} \end{pmatrix}, |u_v\rangle = \begin{pmatrix} -\sin \frac{\theta}{2} \\ e^{i\varphi} \cos \frac{\theta}{2} \end{pmatrix},$$

where

$$\Delta' = \Delta - \lambda_v \tau s_z, \tan \theta = \frac{2atk}{\Delta'}, \tan \varphi = \frac{k_y}{k_x}.$$

Considering an optical interband transition from the upper valence band to the bottom of the conduction band, the coupling strength with the circularly polarized light can be estimated by the interband components of the canonical momentum operator:

$$P_{\pm}(k) = \frac{m_0}{\hbar} \langle u_c | \left(\frac{\partial \hat{H}}{\partial k_x} \pm i \frac{\partial \hat{H}}{\partial k_y} \right) | u_v \rangle$$

Near the K point,

$$|P_{\pm}(k)|^2 = \left(\frac{m_0 at}{\hbar} \right)^2 \left(1 \pm \tau \frac{\Delta'}{\sqrt{\Delta'^2 + (2atk)^2}} \right)^2$$

Because $\Delta' \gg atk$, the circularly polarized light strongly couples to one of the two valleys exclusively. Considering the conduction band fine spin-splitting due to inter-atomic SOC, the optical selection rule derived above enables us to selectively excite the electron in one valley. Eventually, we can generate a

pair of excited electrons and residual holes which are spin-polarized in the mutually opposite direction with the circularly polarized light.

2.1.3. Exciton in Monolayer TMD

Photoexcited electrons in the conduction band and residual holes in the valance band can form a quasi-particle called exciton as a result of Coulomb interaction between them. Inside a 3D bulk material, the Coulomb interaction between electron and hole is reduced by a dielectric environment. In contrast, the interaction is much bigger in 2D material than in 3D case because the electric field lines stretching from hole to electron extend outside of the material so that the dielectric screening becomes much smaller. Excitons in TMD monolayer have the binding energy of a few hundreds of meV, enabling the excitonic effect even at room temperature. Since TMD monolayer has a direct bandgap, oscillator strength of the excitonic resonance is strong in photoluminescence (PL) as well as optical absorption (or reflection contrast (RC)) spectrum [9].

There're many kinds of exciton complexes that can be observed in monolayer TMD such as dark exciton, intervalley exciton, exciton phonon replica states, biexciton, and their charged forms. Exploiting the two-dimensional nature, the charge carrier density of monolayer TMD can be easily tuned by fabricating a capacitor structure so that the physical properties of these exciton complexes can be studied thoroughly. In this study, we are interested in the A exciton and charged exciton of

monolayer MoSe_2 . The charged exciton is called trion which indicates a bound state of an A exciton in one valley and a charge carrier in the other valley. But this scheme lacks consideration of many-body interaction between exciton and Fermi sea consisting of charge carriers. Thus, many research groups recently call the charged A exciton “attractive exciton-polaron” and the original A exciton branch “repulsive exciton-polaron”. We aren’t much interested in the many-body effect of the charged exciton, so let’s call it trion.

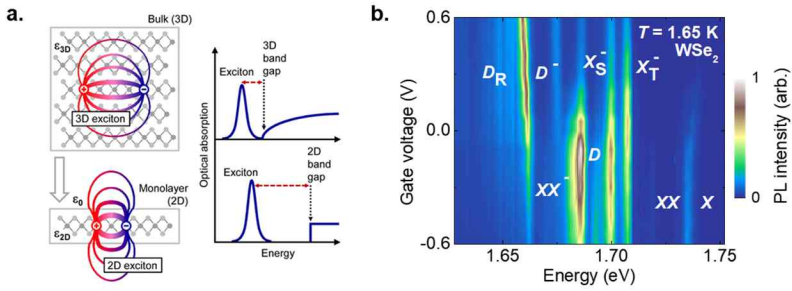


Figure 19 a. Schematics of excitons in real space and optical absorption spectra in 2D & 3D cases [10]. b. Gate dependent PL of monolayer WSe_2 .

2.2. van der Waals Magnets

There’re various kinds of van der Waal magnets with many kinds of magnetic order linked to their band structures. The properties of the magnet itself such as topological insulator [11], magnon [12], and topological spin-defect [13] are actively studied recently. Their potential as the component of the magnetism-based electronic device is also under a wide range of research by fabricating van der Waals heterostructures. In this

study, we are especially interested in chromium tribromide which is in a class of a chromium trihalides.

2.2.1. Chromium Trihalides

Chromium trihalide refers to a class of van der Waals magnet that has the chemical formula of CrX_3 , where X is a halide element: I, Br, or Cl. In this kind of material, d-orbitals of central chromium ion (Cr^{3+}) are energy-split under an octahedral field into upper e_g orbitals and lower t_{2g} orbitals. In the ground states, following Hund's rule, three electrons in d-orbitals occupy these t_{2g} orbitals and have the same spin orientation, which is the origin of magnetism. It has intralayer ferromagnetism originating from the super-exchange interaction through the Cr-X-Cr path [14]. The interlayer magnetism which comes from the super-exchange coupling through the Cr-X-X-Cr path is tunable by the stacking order of layers. A chromium tribromide, which is the key material of this study, has perpendicular magnetic anisotropy for a monolayer form and its few-layer-form has ferromagnetic coupling for the batch grown by chemical vapor deposition.

Speaking of optical transitions, chromium trihalides have an indirect bandgap in the NIR range. The lowest two absorption resonances are d to d transitions in which electrons are transferred from t_{2g} orbital to e_g orbital. (${}^4A_{2g} \rightarrow {}^4T_{2g}$, ${}^4A_{2g} \rightarrow {}^4T_{1g}$) Under the Laporte rule, such d to d transition is electric-dipole-forbidden for centrosymmetric system and can only weakly come into play by an anisotropic phonon, a trigonal

field of near Cr atoms or Jahn–Teller distortion, etc. Main absorption resonance is in the visible range and called “ligand to metal charge transfer” (LMCT), which means optical transitions from 3p orbitals of ligand atoms to 3d orbitals of metal atoms. Due to spin–split bands, we can estimate the magnetic dipole moments through circular dichroism measurements using light whose wavelength is around LMCT resonances. This kind of measurement is called magnetic circular dichroism (MCD)

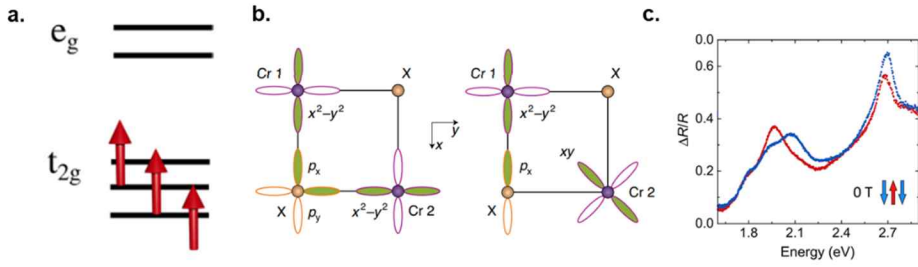


Figure 3 a. Electron spin configuration in d orbital of Cr^{3+} in CrX_3 [15]. b. Schematics for intralayer super–exchange interaction in CrX_3 [14]. c. Circular–polarization–resolved reflection contrast spectrum of tri–layer CrI_3 [16].

Chapter 3. Methods

3.1. Device Fabrication

The electrically tunable van der Waals heterostructures of monolayer MoSe₂ and 3–20 nm thick CrBr₃ were fabricated through several steps of polycarbonate (PC) film–based transfer, nano–squeegee [17], and electron beam lithography. The CrBr₃, a member of chromium trihalides, is notorious for its rapid decomposition by photocatalytic reactions with moisture, and therefore requires complete encapsulation for handling in the air [18, 19, 20]. Thus, to keep both sides of CrBr₃ atomically clean and to make a reliable electrical connection, the following series of processes were performed.

1. Exfoliation of hexagonal boron nitride (hBN), few–layer graphene (FLG), monolayer MoSe₂, 3–5 nm CrBr₃ onto Si/SiO₂ wafer
2. Transfer of bottom hBN (Fig. 4a)
 - a. Pick up and transfer the hBN flake onto the Si/SiO₂ substrate prepared with pre–patterned Ti (10 nm)/Au (250 nm) electrodes via dry transfer technique using PC/PDMS stamp.
 - b. Heat clean at 200 °C for 6+ hours in forming gas (H₂ + Ar).
3. Transfer of two FLG (Fig. 4b)
 - a. Pick up two FLG sequentially and transfer the flakes onto the bottom hBN as steps 1 (a)
 - b. Heat clean at 200 °C for 6+ hours in forming gas.
4. Creation of contact electrodes

- a. Spin-coat and bake of PMMA resist.
 - b. Electron beam lithography to define contacts.
 - c. Develop resist in water – IPA mixture. (Fig. 4c)
 - d. Deposit Ti (15 nm)/Au (285 nm) in a thermal evaporator.
 - e. Liftoff by immersion into acetone. (Fig. 4d)
 - f. Heat clean at 200 °C for 6+ hours in forming gas.
 5. Formation and transfer of MoSe₂/CrBr₃ heterostructures
 - a. Pick up and transfer top hBN onto the exfoliated monolayer MoSe₂ as steps 1 (a) (Fig. 4f)
 - b. Perform a nano-squeegee for hBN/MoSe₂ with a typical setpoint of 2000–5000 nN (PPP–NCHR: 42 N/m) in contact mode using an atomic force microscope (Park Systems, NX10).
 - c. Pick up hBN/MoSe₂ and CrBr₃ sequentially and transfer the flakes onto the prepared FLG/hBN substrate as steps 1 (a) (Fig. 4g–h)
- *This step was performed inside a glovebox filled with argon gas with less than 0.1 ppm oxygen and moisture.

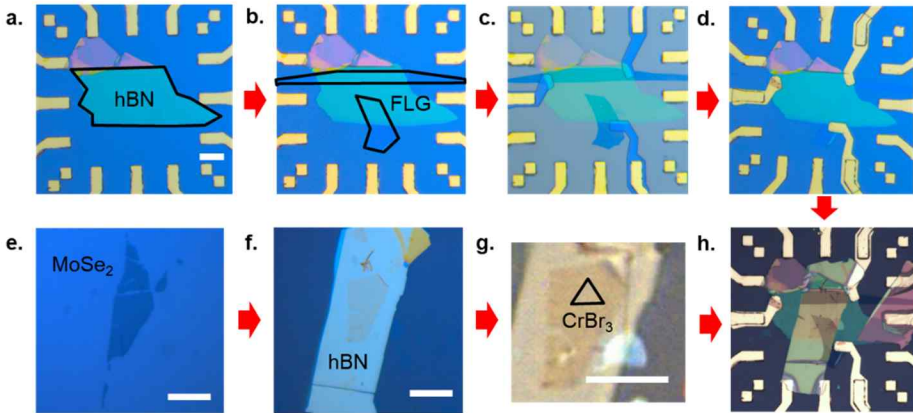


Figure 4 Optical microscope images for device fabrication steps. White scale bars represent 20 μm. a. Transfer of bottom hBN. b. Transfer of FLG. c. Electron beam lithography and

development of PMMA resist. d. Thermal evaporation of Ti/Au contact and lift-off. e. Exfoliation of monolayer MoSe₂. f. Transfer of top hBN. g. Pick up of CrBr₃. h. Finished device.

3.2. PL, RC and MCD Measurements

All the optical measurements in this study were performed in a Faraday geometry at a closed-cycle cryostat equipped with a superconducting magnet (attocube, attoDRY 2100), which offers a continuous base temperature of 1.65 K and a magnetic field up to 9 T. At the top of the insert, there are a transparent window and SMA connectors which enable both optical and electrical approaches to the sample at the lower part of the insert. We add an optical breadboard on the cryostat so that we can freely organize optical experiments. We constructed a scanning system with a pair of galvo mirrors (Thorlabs, GVS012) and 4f lenses (AC254-400, AC254-500). CCD camera, broadband LED, and two beam splitters between the galvo mirrors and 4f lenses enable us to easily check the sample & beam position.

For PL measurements, we introduced a single-mode fiber-coupled 633 nm laser diode (HL63163DG) with a power stabilization system utilizing an acousto-optic modulator (ISOMET, M1205-P80L-3 & 630C-80) to suppress the fluctuations of beam pointing and long-term drift of laser power. The 633 nm PL pump beam from the single mode fiber was collimated by a triplet collimator (TC18FC-633), transmitted through a linear polarizer (GL10-B), and injected into the beam splitter (BSS10R) so that the power of the reflected beam was

measured by a power meter (S120C & PM100D) for feedback power control. The transmitted beam from the beam splitter was reflected from a long-pass dichroic mirror (DMLP650) and then focused onto the sample by an objective with a numerical aperture of 0.82 (attocube, LT-APO/VISIR) into $< 1 \text{ } \mu\text{m}$ spot size. The reflected light from the sample was collected by the same objective, transmitted through the dichroic mirror, and coupled to a multimode fiber of $50 \text{ } \mu\text{m}$ diameter. The emitted light from the optical fiber was split by a fiber beam splitter, and then one-half of it was spectrally resolved by a monochromator (Dongwoo Optron, MonoRa500i) and detected by a TE-cooled CCD camera (Andor, Newton920). The other half of the light went into the single photon counter module (SPCM) (EXCELITAS, SPCM-AQRH-14-FC) and the signal from it was read by photon counter electronics (Stanford Research Systems, SR400). Since the SPCM can measure the real-time total PL counts, we could utilize the SPCM signal for fine alignments of fiber coupling or spatial fast-mapping of the total PL signal.

Because the multimode fiber for detection serves as a spatial filter, our setup defines confocal microscopy so that we could obtain a spatial resolution of less than $1 \text{ } \mu\text{m}$ for PL spatial mapping using the galvo mirror.

$$D = \frac{\lambda f}{r}$$

(D is a diffraction-limited spot size at the 99% contour, λ is a wavelength of light, f is a focal length of the focusing lens for fiber coupling, and r is an input beam radius.) For $65 \text{ } \mu\text{m}$ spot size, 750 nm wavelength and 2 mm beam radius, the optimal focal length of the focusing lens is 170 mm . We introduced a 150

mm achromatic lens for detection (AC254-150-B).

For circular-polarization-resolved PL measurements, an achromatic quarter-wave plate (QWP) (AQWP05M-600) was introduced into the common path of excitation and detection. The linear polarized PL pump was circularly polarized by the QWP whose fast axis was 45° tilted with respect to the PL pump polarization. Then, as the emitted PL signal was transmitted through the QWP, the right(left)-circularly polarized component from the sample changed its polarization to co(cross)-linearly polarized component with respect to the initial PL pump polarization. Thus, by adjusting the PL pump polarization to the p(s)-polarization with respect to the dichroic mirror, we could minimize the polarization mixing. We introduced an achromatic half-wave plate (HWP) (AHWP05M-600) and a linear polarizer (GL10-B) into the detection path so that we could eventually choose one of the circularly polarized components of the PL signal. Practically, the retardance of the QWP(HWP) is not 0.25(0.5) and is wavelength-dependent. Therefore, fine-tuning of the fast axis angle of it was performed by exploiting the valley polarization of the monolayer MoSe_2 PL signal in a zero magnetic field or the valley Zeeman splitting of it in a finite magnetic field.

For RC measurements, a halogen lamp (OSL2) was used as a white-light source. The output of the lamp was collected by a single mode fiber, collimated by a triplet collimator (TC18FC-780), and linearly polarized by a linear polarizer (GL10-B). Then the light was reflected from a beam splitter (BSW26R) and focused onto the sample with the same objective as in the PL measurements. The reflected light was collected by the same objective, transmitted through the beam splitter, spectrally

resolved by the monochromator, and detected by the CCD camera. Unlike the PL measurements, we chose a free space optical path for detection because the multimode fiber gives polarization fluctuation and spatial interference. We have obtained the spectral fluctuation of 5% at best when using the multimode fiber for detection. The RC signal seems to be inherently sensitive to spectral fluctuation. By introducing the free space detection, we excluded such fluctuations coming from the optical fiber so that we could achieve spectral fluctuation of less than 1% and long-term drift of less than 0.5% per hour.

For circular polarization resolved RC measurements, the QWP was introduced into the common path of injection and detection. Since the power of the injected light was kept to less than 100 nW, the cross-polarized component of the reflected light was negligible. Thus, we didn't use any polarizer for the detection path.

The reflection contrast spectrum was obtained by detecting the spectrum of light reflected from the sample (R) and the substrate next to the sample (R_0) and calculating $\Delta R/R_0 = (R - R_0)/R_0$

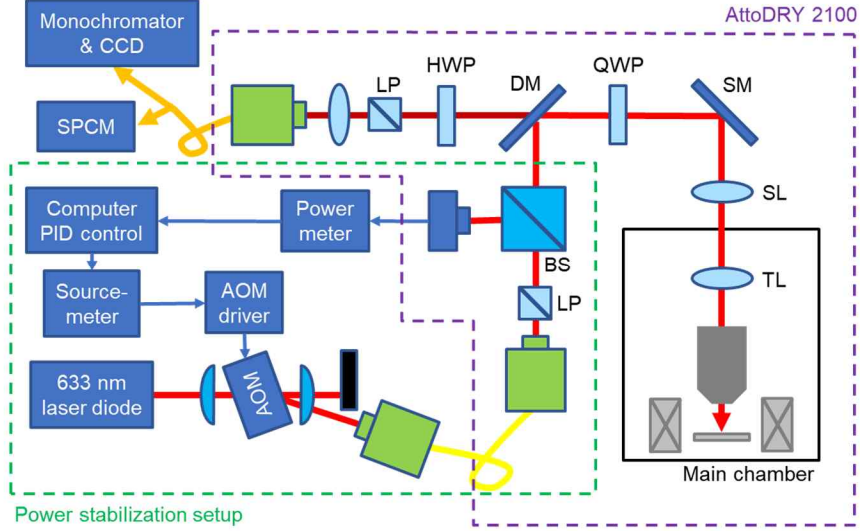


Figure 5 Schematics of an experimental setup for a magnetic-field-dependent circular-polarization-resolved PL. LP: linear polarizer, DM: dichroic mirror, SM: scanning mirror, SL: scan lens, TL: tube lens, BS: beam splitter.

For MCD measurements, we coupled the light emitted from a 405 nm laser diode (DL5146-101S) into a single mode fiber and collimated the output by a triplet collimator (TC18FC-405). Putting linear polarizer (GL10-A, 0° tilted), HWP (22.5° tilted), and photo-elastic modulator (PEM, Hinds Instruments, PEM100, 0° tilted) in sequence, we modulated the polarization of light in the manner of quarter-wave mode ($f = 50$ kHz) as depicted in Fig. 6b. Then the amount of reflected light was detected by SPCM. We introduced a boxcar averaging scheme in which we could selectively open the A(B) gate for right(left)-circularly polarized light. The gate widths were $2 \mu\text{s}$ for both gates. Since SPCM is a sensitive detector specialized for single-photon counting, in spite of the large absorbance of 405 nm light for our optical setup (around OD 2-3), we could get signal

fluctuation of less than 1% with an optical power of only $10 \mu\text{W}$.

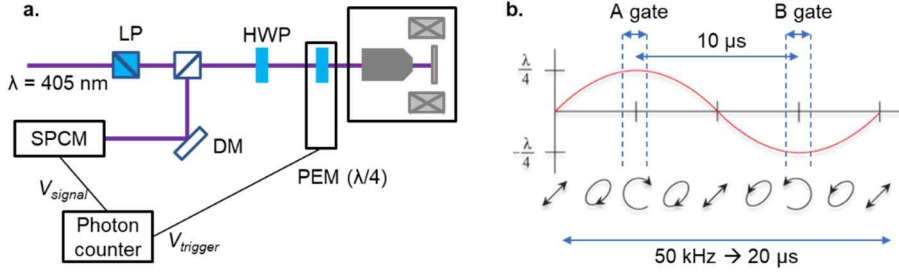


Figure 6 a. Schematics of an experimental setup for MCD measurements. LP: linear polarizer, DM: dielectric mirror. b. Quarter-wave polarization modulation and boxcar averaging scheme with A, B gates.

3.3. TR and TR-KR Measurements

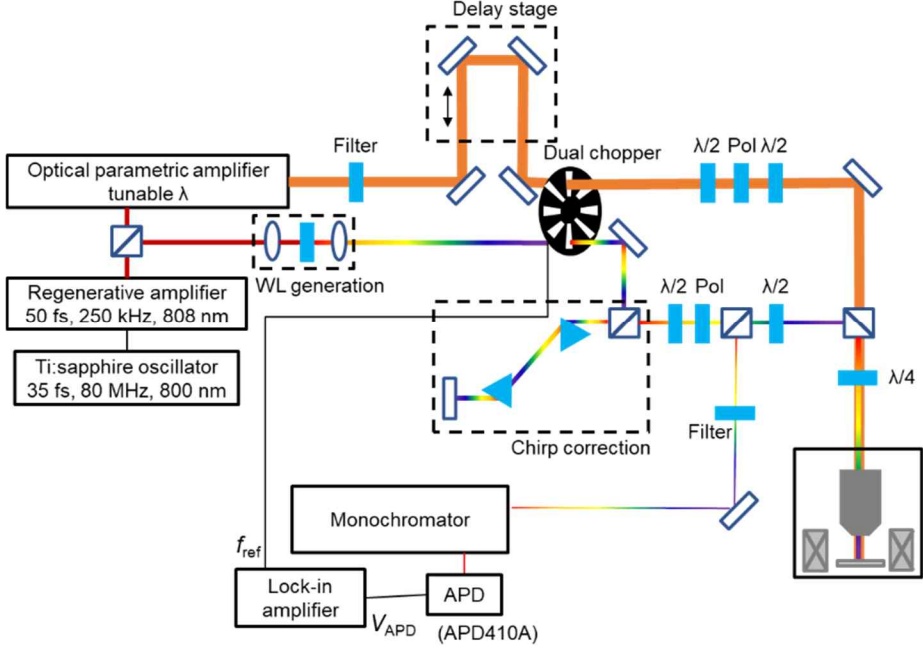
For time-resolved studies, the 250 kHz Ti:sapphire regenerative amplifier laser system (Coherent, RegA 9050) was introduced. 808 nm output of it was split into pump arm and probe arm. A pump pulse of 633 nm was obtained through optical parametric amplification (OPA, Coherent, OPA 9400). The temporal width of the pump pulse at the sample was estimated to be $\sim 300 \text{ fs}$ by the rising time of the pump-probe signal for the reference Bi_2Se_3 sample. Probe pulse with broad spectral bandwidth was obtained through white-light continuum generation utilizing self-phase modulation in sapphire substrate. Through prism pair compensation, we corrected the positive chirps induced by optical elements so that an unchirped pulse was formed at the sample. The pump and probe arms met at the beam splitter and were normally injected into the sample through the objectives. The time delay between pump and probe pulses is manipulated by the mechanical delay stage (Newport, M-

IMS300PP).

For transient reflectivity (TR) measurements, the pump(probe) beam has a spot size of $10\ \mu\text{m}(2\ \mu\text{m})$ and fluence of $100\ \mu\text{J}/\text{cm}^2(500\ \mu\text{J}/\text{cm}^2)$. The reflected light was filtered through a 650 nm long pass filter (FELH0650) to remove the pump beam, spectrally resolved by a monochromator, and detected by an avalanche photodiode (APD, APD410A). With a lock-in amplifier (Stanford Research System, SR830), we measured the probe reflectivity (R) in $f_1=1\ \text{kHz}$ and pump-induced change of it (dR) in $f_2=1.2\ \text{kHz}$, defining a transient reflectivity as dR/R . For the valley-selective pump and probe, we introduced a QWP, two linear polarizers, and four HWPs as depicted in Fig. 7a.

For time-resolved Kerr rotation (TR-KR) measurements, we spectrally filtered the white light with 770 nm center wavelength and 10 nm bandwidth for the probe beam. The pump(probe) beam has a spot size of $10\ \mu\text{m}(5\ \mu\text{m})$ and fluence of $100\ \mu\text{J}/\text{cm}^2(800\ \mu\text{J}/\text{cm}^2)$. The reflected light was filtered through a 650 nm long pass filter (FELH0650) to remove the pump beam, split by the Wollaston prism, and detected by an auto-balanced detector (Newport, Nirvana 2007). The split ratio of signal and reference was controlled at about 1:1.3 for auto-balanced detection.

a.



b.

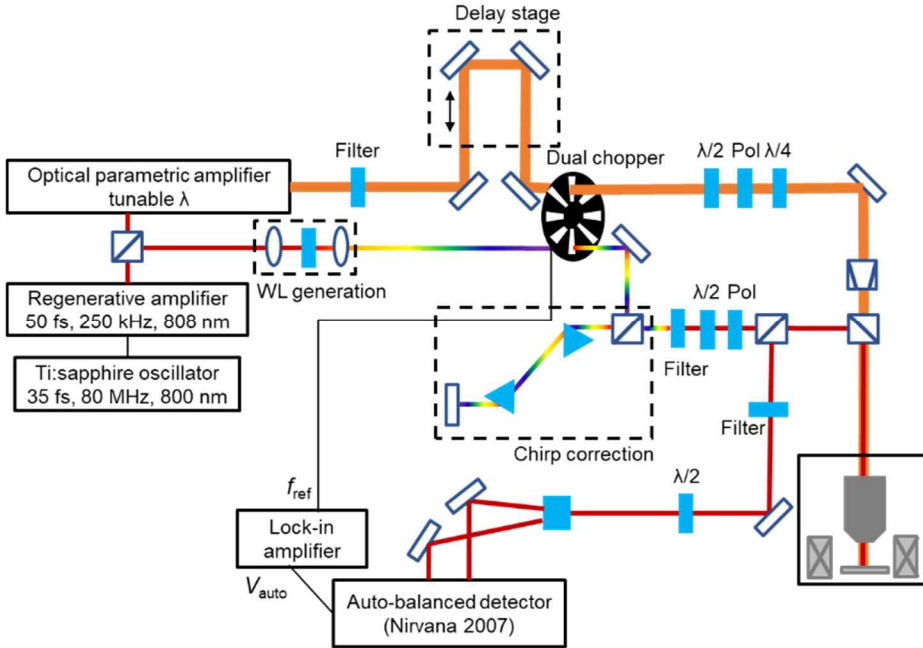


Figure 7 a. Schematics of an experimental setup for TR measurements. b. Schematics of an experimental setup for TR-KR measurements.

Chapter 4. Magnetic Proximity Effect in MoSe₂/CrBr₃ Heterostructures

4.1. Type-II Band Alignment and Spin-selective Charge Transfer

This section is about the results of experiments for device #1.

4.1.1. PL Spectrum

Let's define R/L as the experimental settings with excitation of right circularly polarized light and detection of left circular polarized light. R/R, L/R, and L/L are defined similarly.

*If not specified, note that all the measurements were performed under $T = 1.65$ K, $B = 0$ T, $P = 20 \mu\text{W}$, $V_g = 0$ V, L/L configuration.

The sample consists of a monolayer MoSe₂ in direct contact with 3–5 nm thick CrBr₃ downside encapsulated by hBN of thickness $t_{\text{top}} = 85$ nm, $t_{\text{bottom}} = 25$ nm. And two FLGs are in contact with MoSe₂/CrBr₃ heterostructures as in Fig. 8a so that we can apply an in-plane electric field to the sample as well as an out-of-plane electric field using a silicon back-gate.

We obtained a spatial map of the total PL signal by utilizing a pair of scanning mirrors and an SPCM, and it shows

obvious PL quenching in MoSe_2/FLG and $\text{MoSe}_2/\text{CrBr}_3$ regions (Fig. 8b) Ultrafast transfer of photoexcited charge carrier from the monolayer MoSe_2 to the (semi-)conductive materials defines non-radiative relaxation channels for conduction band electrons and excitons in MoSe_2 , which reduces the total PL signal. We checked the PL spectra of several spots and confirmed that most of the area of CrBr_3 had been already decomposed. This can also be verified by the spatial map of magnetic domains as in Fig. 11. The product of CrBr_3 degradation is known to be a conductive aqueous solution of chromium ions, which explains why the total PL signal in the regions with non-decomposed CrBr_3 is stronger than the ones with decomposed CrBr_3 . In this study, we focused on the spectrum of the $\text{MoSe}_2/\text{CrBr}_3$ heterostructures with non-decomposed CrBr_3 .

Fig. 8d shows the spectra of monolayer MoSe_2 and $\text{MoSe}_2/\text{CrBr}_3$ heterostructures. The PL spectrum of the heterostructures has an intensity that is about 15 times smaller than that of a monolayer. In addition, the additional non-radiative channel due to charge transfer clearly shows the broadening of the PL linewidth. Since the monolayer was originally lightly n-doped, the two peaks of the monolayer spectrum can be designated as a negative trion (T(negative)) and an exciton (X), respectively. On the other hand, due to the type-II band alignment of $\text{MoSe}_2/\text{CrBr}_3$ heterostructures as depicted in Fig. 8c, the peak on the low energy side of the heterostructure is assumed to be a positive trion (T(positive)), which becomes clear when looking the power-dependent PL (Fig. 8e). When the lightly n-doped monolayer MoSe_2 comes into contact with CrBr_3 , electron transfer occurs from MoSe_2 to CrBr_3 , and Fermi energy

is located inside the MoSe₂ bandgap. This can also be confirmed in the gate-dependent RC of heterostructure (Fig. 12). Therefore, the exciton prevails in the spectrum in low power excitation. As the PL pump power increases, due to the fast electron transfer, the residual hole population in the valance band of MoSe₂ increases, resulting in the increasing proportion of the positive trion.

Note that we can guarantee that our 633 nm laser was barely absorbed by CrBr₃ because the energy of the laser lies at the absorption edge between ⁴T₁ resonance and ⁴T₂ [21, 22]. We could not observe the CrBr₃ PL under 633 nm excitation which is known to lie around 920 nm, which corroborates that the laser wasn't absorbed by CrBr₃. This excludes the hole tunneling from CrBr₃ into MoSe₂.

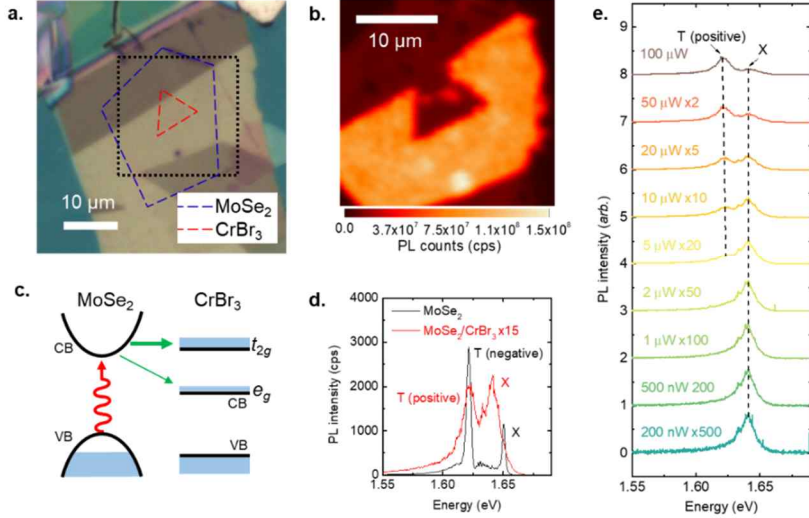


Figure 8 a. Optical microscope image of device #1. b. SPCM scan image of total PL signal. c. Schematics of band alignments and photodoping mechanism. d. PL spectra of monolayer MoSe₂ and MoSe₂/CrBr₃ heterostructures. e. Power-dependent PL spectra of MoSe₂/CrBr₃ heterostructures.

4.1.2. Magneto-PL Spectrum

By varying out-of-plane magnetic fields, we measured the spectrum of the heterostructures. We observed a sharp change in the spectrum near $B = \pm 20$ mT. Fig. 9a shows the magnetic-field-dependent circular polarization-resolved PL spectrum and one can notice the sudden decrease (increase) of the trion PL intensity in the R/R(L) configuration. In contrast, the exciton PL intensity showed no noticeable change.

To explore the change thoroughly, we define the degree of circular polarization (DOCP) as follows for both R and L excitations.

$$\text{DOCP} = (I_R - I_L)/(I_R + I_L)$$

Fig. 9b shows the DOCP map in R and L excitation respectively. One can notice the sign flip of trion DOCP during the magnetic field sweep. The magnetic-field dependence of the exciton DOCP is hardly seen, and it is red for R excitation and blue for L excitation, which implies the non-vanished effect of excitation polarization on the valley polarization. As the R and L excitation show the same pattern for the trion, it can be seen that the sign flip of DOCP is related to the magnetization of CrBr_3 .

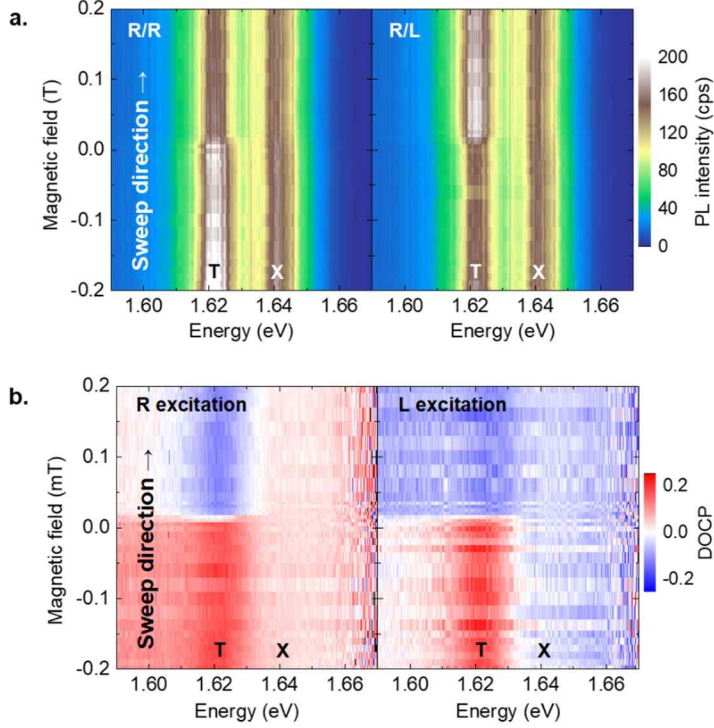


Figure 9 Magnetic-field-dependent circular-polarization-resolved PL of an upward sweep. a. PL map in R/R and R/L configuration. b. DOCP map with R and L excitation.

We fit the PL spectra with the following function of 7 parameters which consists of an exponentially modified Gaussian (exGaussian) distribution and a bare Gaussian distribution.

$$\begin{aligned}
 f(x; A_1, \mu_1, \sigma_1, \lambda, A_2, \mu_2, \sigma_2) &= \frac{A_1 \lambda}{2} e^{\lambda(x - \mu_1) + \frac{1}{2} \lambda^2 \sigma_1^2} \operatorname{erfc}\left(\frac{x - \mu_1 + \lambda \sigma_1^2}{\sigma_1 \sqrt{2}}\right) \\
 &+ \frac{A_2}{\sqrt{2\pi\sigma_1^2}} e^{-\frac{(x - \mu_2)^2}{2\sigma_2^2}}
 \end{aligned}$$

We introduce the exGaussian function to fit the trion low energy tail signal, which has been attributed to the signal originating from some defects or trion recoil effect [23, 24].

We extract the DOCP and the valley splitting using the parameters A_i and μ_i (Fig. 10b, c). The trion resonance shows a clear hysteresis loop about the magnetic field sweep in both DOCP and valley splitting, implying a ferromagnetic phase transition comes into play. In contrast, the hysteresis loop of exciton resonance is less prominent. According to the density functional theory (DFT) calculation of the previous study, resonant tunneling of photoexcited electrons occurs between spin-polarized t_{2g} states of the CrBr_3 conduction band and valley states of MoSe_2 spin-aligned to them [2]. And due to fast valley depolarization outside the light cone in the exciton dispersion, any valley polarization induced by interlayer tunneling at higher energy will be vanished [25,26]. Therefore, regardless of the polarization of the excitation laser, most of the emitted PL becomes circularly polarized with respect to the valley whose conduction band is spin-aligned to e_g states of the CrBr_3 conduction band. This mechanism is depicted in Fig. 10a. The DFT calculation predicted that the conduction band energy with spin-aligned to e_g states of the CrBr_3 conduction band is higher than those with spin-reversed. This is contradictory to the experimental results where DOCP and valley splitting have the mutually opposite sign. The contradiction may be attributed to the excitonic effect such as binding energy and exchange energy. The obscureness of DOCP for exciton resonance implies that the charge transfer timescale is somewhere between the exciton radiative lifetime, which is sub-ps [27], and the trion radiative lifetime, which is ten few ps [28].

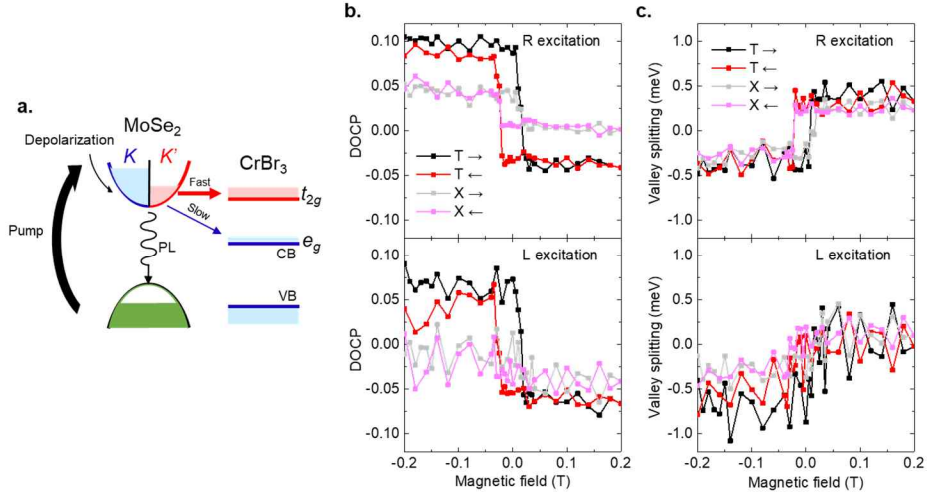


Figure 10 a. Schematics of spin-dependent charge transfer from MoSe₂ into CrBr₃. b. Magnetic-field-dependent DOCP of trion and exciton with R excitation and L excitation. c. Magnetic-field-dependent valley splitting of trion and exciton with R excitation and L excitation.

4.1.3. Magnetic Domain Mapping with PL Signal

Making use of the dependence of DOCP on the CrBr₃ magnetization direction, we could map the magnetic domain by scanning the DOCP of the total PL signal with SPCM (Fig. 11). The blue (red) regions under the R (L) excitation indicate the spin up (down) domain. As can be seen, there was sizable degradation so the PL signal from most areas of the heterostructures shows the valley polarization of the excitation polarization.

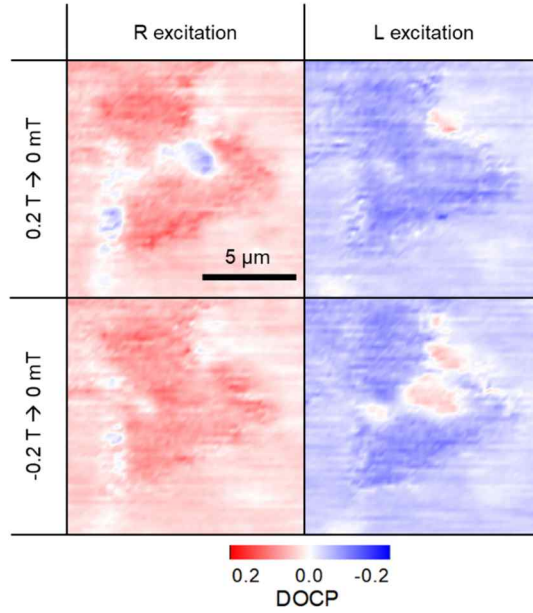


Figure 11 SPCM scan image of DOCP of total PL signal.

4.1.4. RC Spectrum

Fig. 12 shows the results of RC measurements for the monolayer MoSe_2 region and the $\text{MoSe}_2/\text{CrBr}_3$ hetero-region. Due to the type-II band alignment of MoSe_2 and CrBr_3 , the RC spectrum of the heterostructures shows only the exciton resonance (Fig. 12c) while varying the electron density from the lightly n-doped region to the heavily n-doped region in the monolayer (Fig. 12a). We didn't observe any signatures of valley splitting in the circular-polarization-resolved RC spectrum (Fig. 12b). For some reasons, clearness of the valley splitting in the RC spectrum depends on the thickness of CrBr_3 . Note that the previously reported magnetic proximity in RC measurements of $\text{MoSe}_2/\text{CrBr}_3$ heterostructures consists of a monolayer MoSe_2 and a bilayer or penta-layer CrBr_3 [2, 29].

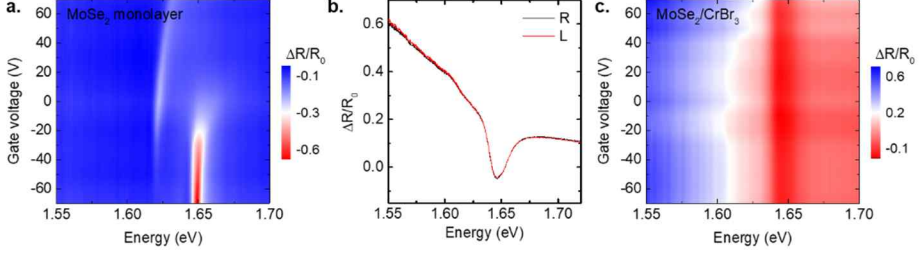


Figure 12 a. Gate-dependent RC spectrum of monolayer MoSe₂. b. Circular polarized resolved RC spectrum of MoSe₂/CrBr₃ heterostructures at $B = 200$ mT. c. Gate-dependent RC spectrum of MoSe₂/CrBr₃ heterostructures at $B = 200$ mT.

4.2. Antiferromagnet-like Switching and Charge Transfer-dominated DOCP

This section is about the results of experiments for device #2.

4.2.1. Magneto-PL spectrum

After finding out that excitation polarization doesn't affect the polarization of photoluminescence, we applied excitation of linear polarization for device #2.

The sample consists of a monolayer MoSe₂ in direct contact with 10–20 nm thick CrBr₃ downside encapsulated by hBN of thickness $t_{\text{top}} = 55$ nm, $t_{\text{bottom}} = 15$ nm. We obtained a spatial map of the total PL signal and it shows obvious PL quenching in MoSe₂/CrBr₃ regions (Fig. 13b). Through the PL DOCP map in Fig. 13c, we can notice that the DOCP sign flip three times per sweep. We fit the PL spectra in the same manner as

for device #1 (Fig. 13d). As in 4.1.2., the trion resonance shows clear magnetic-field dependence while the exciton resonance has negligible dependence. This kind of multiple domain flip was reported in van der Waals materials for Hall bar magnetometry of CrBr_3 magnetization or PL ρ of $\text{WSe}_2/\text{CrI}_3$. Since PL DOCP is related to spin-selective charge transfer from MoSe_2 to CrBr_3 rather than real magnetic flux near the MoSe_2 monolayer, we can say that our situation is different from the former CrBr_3 case. For the latter $\text{WSe}_2/\text{CrI}_3$ case, [1] interpreted the multiple hystereses as competition between strong- and weak-ferromagnetic domain while [30] interpreted it as the flipping of the topmost layer with antiferromagnetic interlayer coupling.

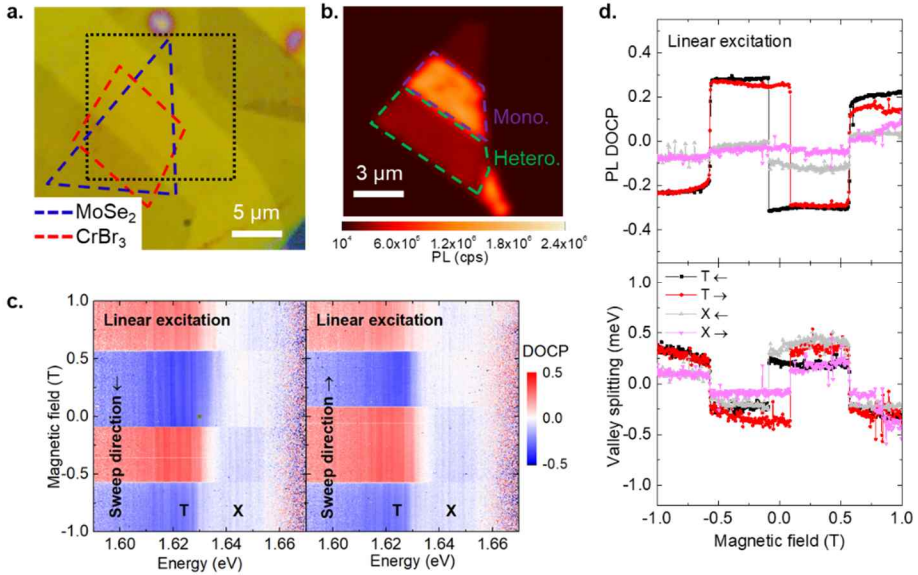


Figure 13 a. Optical microscope image of device #2. b. SPCM scan image of total PL signal. c. DOCP map with linear polarized excitation. d. Magnetic-field-dependent DOCP and valley splitting of trion and exciton with linear polarized excitation.

4.2.2. Magnetic Domain Characterization

To confirm whether there is somehow antiferromagnetic interlayer coupling or not, we obtained an MCD hysteresis loop for a point in the middle of the heterostructures (Fig. 14a). We mark the data points where the DOCP sign flips with grey vertical dashed lines. Note that the MCD loop implies that increasing magnetic field leads to the strengthening of CrBr₃ magnetization, while DOCP changes in a mutually different direction for $B = \pm 90$ mT and ± 575 mT. Besides, one can notice there're many points where the MCD value changes while PL DOCP remains constant. We checked DOCP observed was uniform throughout the heterostructures (Fig. 14b). Therefore, these findings suggest that there's antiferromagnetic interlayer coupling so that MCD and DOCP behave differently for magnetic field sweep. This is contradictory to what has been previously reported that CrBr₃ is ferromagnet. Many factors such as strain, partial degradation, and twist angle can be considered as the cause of making CrBr₃ partial antiferromagnet. Second harmonic generation may occur due to inversion symmetry breaking by interlayer antiferromagnetic order, and it needs to be investigated [31].

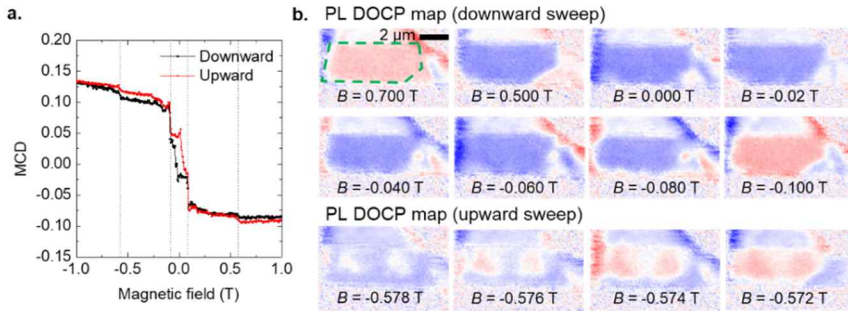


Figure 14 a. MCD hysteresis loop. b. PL DOCP map with linear polarized excitation for several magnetic fields.

4.2.3. Charge–transfer–dominated DOCP

Fig. 15 shows PL DOCP and valley splitting for magnetic field sweep from -8 T to 8 T. Recently, gate– and magnetic–field–dependent DOCP of hBN–encapsulated monolayer MoSe_2 has been reported [32]. With a large magnetic field applied, the valley polarization of electron(hole) evolves for negatively(positively) doped MoSe_2 due to valley Zeeman splitting. For negatively(positively) doped MoSe_2 , DOCP of exciton has the same(opposite) sign with valley splitting, and one of trion has the opposite(same) sign with valley splitting. Based on the argument above, the evolution of exciton DOCP follows the tendency of positively doped MoSe_2 . In contrast, the DOCP of trion depends on CrBr_3 magnetization and is nearly constant for a large magnetic field. The DOCP sign of $\text{MoSe}_2/\text{CrBr}_3$ we obtained is the opposite to one of MoSe_2 reported. We can notice that the observed trion DOCP is dominated by charge transfer dynamics. In addition, the weak dependence of exciton DOCP on CrBr_3 magnetization implies that sizable static valley hole polarization is implausible.

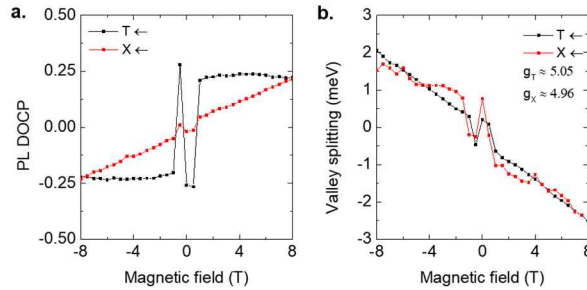


Figure 15 Large–field–dependent a. PL DOCP and b. valley splitting.

Chapter 5. Ultrafast Studies on Carrier Dynamics in MoSe₂/CrBr₃ Heterostructures

5.1. TR Measurements

Ch.5 is devoted to the time-resolved experiments for device #2.

To analyze the charge transfer dynamics in MoSe₂/CrBr₃ heterostructures, we obtained the TR spectrum for both MoSe₂ monolayer and MoSe₂/CrBr₃ heterostructures (Fig. 16a, d). Due to the multireflection effect from the surrounding hBN and SiO₂ layer, we need to consider the reflectivity spectrum of the complex line shape when evaluating the TR spectrum. Applying the TR spectrum at $t = 1$ ps to sample reflectivity, we modify the RC spectrum. Fig. 16b, e show a reduction of oscillator strength and slight redshift of exciton resonance, which is the result of photobleaching and photo-induced absorption. Thus, the TR signal here contains information on the modification of exciton resonance due to carrier dynamics. Time-delay-dependent pump-probe signal of MoSe₂/CrBr₃ at low energy wing of exciton resonance shows a long-lasting residual signal, which is unlike for MoSe₂ monolayer (Fig. c, f). In MoSe₂/CrBr₃ heterostructures, after the pump-induced electron-hole plasma formation and exciton formation process, the charge transfer pathway for electrons leaves holes in MoSe₂. These holes are free from exciton recombination dynamics, which leads to a long lifetime. Although we searched for a circular-polarization-

dependent TR signal indicating valley-selective excitation or spin-selective charge transfer, we could not find one within the resolution range that the optical stability of our setup permitted.

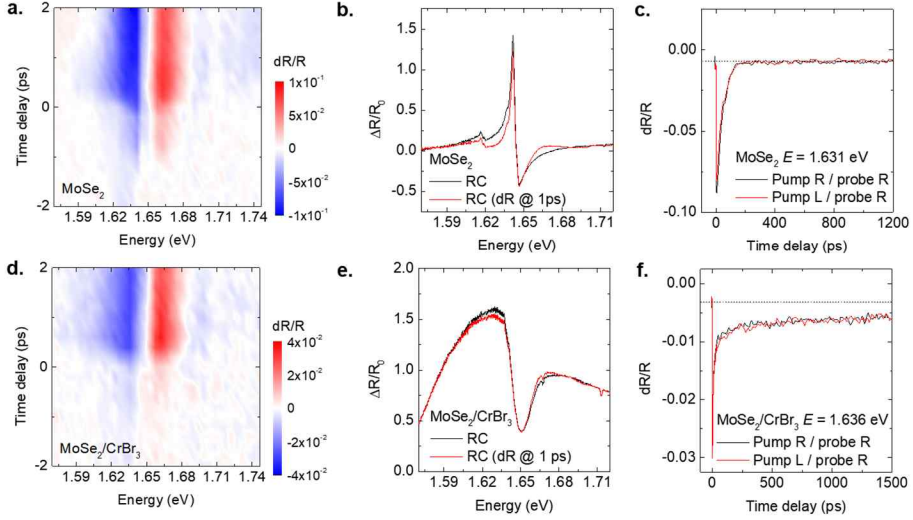


Figure 16 a. TR spectrum for monolayer MoSe_2 . b. RC spectrum raw data and one modified by TR spectrum at $t = 1$ ps for monolayer MoSe_2 . c. TR at low energy wing of exciton resonance for monolayer MoSe_2 . d–f. Figures of the same forms with a–c for $\text{MoSe}_2/\text{CrBr}_3$ heterostructures.

5.2. TR–KR Measurements

Exploring the valley-related signal, we performed TR–KR measurement which is sensitive to valley imbalance of charge carrier. Fig. 17a shows the raw data of the time–delay–dependent auto–balanced signal. Due to the low reflectivity of the probe from the sample, we could not reject the common mode signal (dR/R) enough. In other words, we had a poor common mode rejection ratio (CMRR). Therefore, the only differential TR–KR between different experimental conditions is meaningful.

The differential TR–KR between different polarizations shows the rate with which the pump–induced valley information erases (Fig.17 b, c). Note that the signals die out within 1 ps both in MoSe₂ monolayer and MoSe₂/CrBr₃ heterostructures. It implies that the valley depolarization time in MoSe₂ is < 1 ps, which would be smaller than exciton & trion radiative lifetime and overall charge transfer time. We searched for the differential TR–KR between different CrBr₃ magnetization directions, and we didn't succeed. Spin–selective charge transfer is expected to create a valley imbalance in the timescale of the faster route. Our TR–KR results imply that such residual signal is smaller than the resolution of our optical setup.

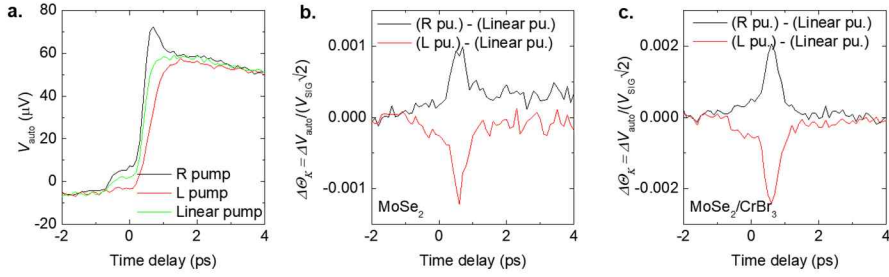


Figure 17 a. Raw data of time–delay–dependent auto–balanced signal. b. differential TR–KR for monolayer MoSe₂. c. differential TR–KR for MoSe₂/CrBr₃ heterostructures.

Chapter 6. Conclusion

In this study, we fabricated $\text{MoSe}_2/\text{CrBr}_3$ van der Waals heterostructures in a transistor form. By measuring power-dependent PL, we could confirm the observed two features in the PL spectrum of the heterostructures are positive trion and exciton respectively. We designed the circular-polarization-resolved optical setup and performed magneto-PL measurements. We observed the sharp change in the PL intensity of the trion and attributed it to the local magnetization flip of CrBr_3 . It is due to spin-dependent interlayer charge transfer rate and can be used to realize magnetism-based electronic devices. Through spatial magnetic domain characterization through PL DOCP and MCD, we found evidence of unexpected antiferromagnetic coupling for CrBr_3 , and it needs to be further tested.

TR of the heterostructures shows a residual long-lasting signal from the residual hole in MoSe_2 . Valley depolarization reveals through TR-KR measurements to precede other dynamics such as exciton & trion recombination and charge transfer. We could not observe the TR-KR signal of the residual valley hole generated from the spin-selective charge transfer. Combining the information of PL, RC, TR, and TR-KR can be a powerful tool for evaluating the band-alignment and carrier dynamics in TMD-magnet heterostructures.

Bibliography

- [1] D. Zhong *et al.*, Van der Waals engineering of ferromagnetic semiconductor heterostructures for spin and valleytronics *Sci. Adv.* **3**, 1603113 (2017).
- [2] T. P. Lyons *et al.*, Interplay between spin proximity effect and charge-dependent exciton dynamics in MoSe₂/CrBr₃ van der Waals heterostructures *Nat. Commun.* **11**, 6021 (2020).
- [3] X. Xi *et al.*, Ising pairing in superconducting NbSe₂ atomic layers *Nat. Phys.* **12**, 139–143 (2016).
- [4] J. M. Lu *et al.*, Evidence for two-dimensional Ising superconductivity in gated MoS₂ *Science* **350**, 1353–1357 (2015).
- [5] S. Wu *et al.*, Observation of the quantum spin Hall effect up to 100 Kelvin in a monolayer crystal *Science* **359**, 76–79 (2018).
- [6] P. Rivera *et al.*, Intrinsic donor-bound excitons in ultraclean monolayer semiconductors *Nat. Commun.* **12**, 871 (2021).
- [7] G. B. Liu *et al.*, Electronic structures and theoretical modelling of two-dimensional group-VIB transition metal dichalcogenides *Chem. Soc. Rev.* **44**, 2643 (2015).
- [8] D. Xiao *et al.*, Coupled Spin and Valley Physics in Monolayers of MoS₂ and Other Group-VI Dichalcogenides *Phys. Rev. Lett.* **108**, 196802 (2012).
- [9] K. F. Mak *et al.*, Atomically Thin MoS₂: A New Direct-Gap Semiconductor *Phys. Rev. Lett.* **105**, 136805 (2010).

- [10] A. Chernikov *et al.*, Exciton Binding Energy and Nonhydrogenic Rydberg Series in Monolayer WS₂ *Phys. Rev. Lett.* **113**, 076802 (2014).
- [11] M. M. Otrokov *et al.*, Prediction and observation of an antiferromagnetic topological insulator *Nature* **576**, 416–422 (2019).
- [12] J. Cenker *et al.*, Direct observation of two-dimensional magnons in atomically thin CrI₃ *Nat. Phys.* **17**, 20–25 (2021).
- [13] M. Augustin *et al.*, Properties and dynamics of meron topological spin textures in the two-dimensional magnet CrCl₃ *Nat. Commun.* **12**, 185 (2021).
- [14] B. Huang *et al.*, Emergent phenomena and proximity effects in two-dimensional magnets and heterostructures *Nat. Mater.* **19**, 1276–1289 (2020).
- [15] J. L. Lado & J. F. Rossier, On the origin of magnetic anisotropy in two dimensional CrI₃ *2D Mater.* **4**, 035002 (2017).
- [16] T. Song *et al.*, Spin photovoltaic effect in magnetic van der Waals heterostructures *Sci. Adv.* **7**, eabg8094 (2021).
- [17] M. R. Rosenberger *et al.*, Nano- “Squeegee” for the Creation of Clean 2D Material Interfaces *ACS Appl. Mater. Interfaces* **10**, 10379–10387 (2018).
- [18] M. Grönke *et al.*, Chromium Trihalides CrX₃ (X = Cl, Br, I): Direct Deposition of Micro- and Nanosheets on Substrates by Chemical Vapor Transport *Adv. Mater. Interfaces* **6**, 1901410 (2019).
- [19] D. Shcherbakov *et al.*, Raman Spectroscopy, Photocatalytic Degradation, and Stabilization of Atomically

- Thin Chromium Tri-iodide *Nano Lett.* **18**, 4214–4219 (2018).
- [20] M. Galbiati *et al.*, Very Long Term Stabilization of a 2D Magnet down to the Monolayer for Device Integration *ACS Appl. Electron. Mater.* **2**, 3508–3514 (2020).
 - [21] J. F. Dillon, Jr, H. Kamimura, & J. P. Remeika, Magneto-optical properties of ferromagnetic chromium trihalides *J. Phys. Chem. Solids* **27**, 1531–1549 (1966).
 - [22] V. M. Bermudez, & D. S. McClure, Spectroscopic studies of the two-dimensional magnetic insulators chromium trichloride and chromium tribromide—I. *J. Phys. Chem. Solids* **40**, 129–147 (1979).
 - [23] J. W. Christopher, B. B. Goldberg, & Anna K. Swan Long tailed trions in monolayer MoS₂: Temperature dependent asymmetry and resulting red-shift of trion photoluminescence spectra *Sci. Rep.* **7**, 14062 (2017).
 - [24] J. S. Ross *et al.*, Electrical control of neutral and charged excitons in a monolayer semiconductor *Nat. Commun.* **4**, 1474 (2013).
 - [25] M. M. Glazov *et al.*, Exciton fine structure and spin decoherence in monolayers of transition metal dichalcogenides *Phys. Rev. B* **89**, 201302(R) (2014).
 - [26] M. Yang *et al.*, Exciton valley depolarization in monolayer transition-metal dichalcogenides *Phys. Rev. B* **101**, 115307 (2020).
 - [27] T. Jakubczyk *et al.*, Radiatively Limited Dephasing and Exciton Dynamics in MoSe₂ Monolayers Revealed with Four-Wave Mixing Microscopy *Nano Lett.* **16**, 5333–5339 (2016).

- [28] T. Godde *et al.*, Exciton and trion dynamics in atomically thin MoSe₂ and WSe₂: Effect of localization *Phys. Rev. B* **94**, 165301 (2016).
- [29] J. Choi *et al.*, Asymmetric magnetic proximity interactions in MoSe₂/CrBr₃ van der Waals heterostructures arXiv:2206.09958 (2022).
- [30] K. L. Seyler *et al.*, Valley Manipulation by Optically Tuning the Magnetic Proximity Effect in WSe₂/CrI₃ Heterostructures *Nano Lett.* **18**, 3823–3828 (2018).
- [31] Z. Sun *et al.*, Giant nonreciprocal second-harmonic generation from antiferromagnetic bilayer CrI₃ *Nature* **572**, 497–501 (2019).
- [32] Y. Wu *et al.*, Negative valley polarization in doped monolayer MoSe₂ *Phys. Chem. Chem. Phys.* **24**, 191–196 (2022).

국문초록

2차원 자성체와 전이금속 디칼코게나이드를 결합하여 반데르발스 이중접합구조를 만들면 추가적인 수단으로 밸리 자유도를 제어할 수 있으며 광-밸리트로닉 물질을 기반으로하는 데이터 처리 및 저장을 위한 유망한 플랫폼이 될 수 있다. 이 연구에서 우리는 단층 MoSe_2 와 수 층 CrBr_3 를 접합시켜 반데르발스 이중접합구조를 제작하였다. 빛 세기 의존 광발광 스펙트럼의 측정을 통해서 관찰된 두 개의 공명을 각각 양의 트라이온과 엑시톤으로 할당하였다. 이중접합구조에 대한 원형 편광 분해 자기 광발광 측정을 수행하였고 MoSe_2 트라이온 공명의 밸리 편광이 CrBr_3 자화에 따라 거동하는 것을 관찰하였다. 이것은 MoSe_2 와 CrBr_3 사이의 스핀 의존 층간 전하 이동으로 설명할 수 있다. 게이트 전압 의존 차등 반사율 스펙트럼은 유형-II 밴드 정렬을 확증한다. 우리는 $\text{MoSe}_2/\text{CrBr}_3$ 이중접합 구조에서 광발광 및 자기 원형 양색성 측정을 통해 CrBr_3 에서 예상치 않은 반강자성 결합에 대한 증거를 발견했으며 추가 조사가 필요하다.

이중 접합 구조의 캐리어 역학을 평가하기 위해 과도 반사율과 시분해 커 회전 측정을 수행하였다. 밸리 탈분극 시간은 트라이온과 엑시톤의 복사 수명보다 빠른 1 ps 미만으로 추정되었다. 스핀 의존 전하 이동으로 생성된 잔류 밸리 홀의 커 회전 신호는 확인하지 못하였다.

주요어: 자기 근접효과, 이중접합구조, 자기-광발광, 자기 원형 양색성, 커 회전, MoSe_2 , CrBr_3

학 번: 2020-28149